nature communications

Article

https://doi.org/10.1038/s41467-025-63837-w

Direct synthesis of an iron metal-organic framework antiferromagnetic glass

Received: 10 February 2025

Accepted: 27 August 2025

Published online: 02 October 2025

Check for updates

Luis León-Alcaide[1], Lucía Martínez-Goyeneche[1], Michele Sessolo[1], Bruno J. C. Vieira[2], João C. Waerenborgh[2], J. Alberto Rodríguez-Velamazán[3], Oscar Fabelo[3], Matthew J. Cliffe[4], David A. Keen[5] & Guillermo Mínguez Espallargas[1]

We present a direct route to prepare a family of MOF glasses without a meltable crystalline precursor, in contrast to the conventional melt-quenching approach. This one-step synthesis uses the linker itself as the reaction medium under an inert atmosphere, enabling the incorporation of highly hydrolytically unstable M(II) centers. This route produces high-purity iron (II) MOF glasses avoiding the oxidation and partial degradation commonly associated with the conventional melt-quenching process. The transparent glassy monoliths of formula $Fe(im)_{2-x}(bim)_x$, denoted as **dg-MUV-29** (dg = direct-glass), can be prepared with different amounts of imidazole and benzimidazole as well as with linkers with diverse functionalities (NH_2, CH_3, Br, and Cl). The absence of magnetic impurities allows us to study the magnetic properties of the MOF glass itself and show that MOF glasses are good model systems for topologically-disordered amorphous antiferromagnets. We also present the functional advantages of direct-glass synthesis by creating free-standing films of glassy MOFs and integrating them in optoelectronic devices. Direct-glass synthesis is thus a powerful route to exploit the true functional potential of glassy MOFs, not only realizing further classes of MOF glasses but also unveiling properties that can be accessed with these materials.

Glasses are ubiquitous in our everyday lives, but still pose fundamental questions about the nature of order in solids. Typically formed by the rapid cooling of a liquid, these amorphous solids have broad applications, with vitreous silica (SiO_2) the most well-known example[1]. Most functional glasses are purely inorganic solids, restricting the range of functional properties feasible[2]. Recently, a number of metal-organic framework (MOF) glasses containing molecular components have been discovered by heating their crystalline counterparts to a melting point, followed by a rapid cooling, thereby expanding the potential applications of glass materials[3–5].

MOF glasses combine the unique properties of crystalline MOFs[6,7], such as high surface area and chemical versatility[8], with the distinctive properties of a glass, such as formability[9]. This makes this class of molecular materials particularly interesting for applications that benefit from both porosity and an amorphous nature[10–12], such as advanced gas separation[13,14], hybrid electrochemical systems[15,16], and photonic applications[17].

However, there are currently only a handful of known MOF glasses[3,18], primarily derived from a subclass of MOFs known as zeolitic imidazolate frameworks (ZIFs)[19]. ZIFs are distinguished by their

[1]Instituto de Ciencia Molecular (ICMol), Universidad de Valencia, c/ Catedrático José Beltrán, 2, Paterna, Spain. [2]Centro de Ciências e Tecnologias Nucleares, DECN, Instituto Superior Técnico, Universidade de Lisboa, Bobadela, LRS, Portugal. [3]Institut Laue-Langevin, 71, av des Martyrs, CS 20156, Grenoble, Cedex 9, France. [4]School of Chemistry, University of Nottingham, Nottingham, UK. [5]ISIS Facility, Rutherford Appleton Laboratory, Oxfordshire, UK.
e-mail: guillermo.minguez@uv.es

tetrahedral network structure, which closely resembles that of silica and zeolites[20]. Like silica, these frameworks can melt, and by rapidly cooling the melt, the MOF glass is formed[21,22]. Conversely, unlike silica, the chemical versatility of these molecular-based solids allows the modification of both the metal centers (e.g., Zn, Co, Fe)[23–25] and the organic ligands (e.g., imidazolates, benzimidazolates)[26,27], causing variations in the melting temperatures. Still, the anionic imidazolate is thermally unstable in the temperature regime of melting. This instability means that melt quenching (MQ), even in inert conditions, can introduce impurities into the glass and is particularly acute for MOF glasses with paramagnetic transition metals, which typically contain impurities of metallic cobalt or Fe_3O_4[28,29]. Additionally, thermal processing of MOF glasses requires careful control of the time-temperature process, as melt-quenching rates, re-melting of the glass, or direct collapse of the MOF structure, can have large effects on the final properties of the material, including bubble formation, micro-cracking, surface oxidation, and extent of decomposition[30,31].

Several approaches have been investigated to bypass the melt-quenched process, such as the mechanochemical method, although it has only proven effective with Zn[32]. More recently, the desolvation of metal complexes has been studied to create MOF glasses[33]. In this work, we developed an alternative direct route to MOF glasses, through the reaction of metal precursor and imidazolate ligand[34–36], that does not mirror synthetic routes for traditional inorganic glasses[1], and overcomes the limitations associated with conventional methods for the preparation of molecular-based glasses. Our route allows the preparation of nearly impurity-free MOF glasses containing paramagnetic metals, which permits the exploration for the first time of their intrinsic optical, electronic, and magnetic function. MOF glasses simultaneously possess a long-range structure that is completely disordered, but with a strong short-range order[37]. This mirrors other topologically disordered materials, where the properties such as electronic or photonic band gaps emerge from the local uniformity, as occurs in amorphous silicon or disordered metamaterials[38]. Topologically amorphous antiferromagnets would therefore have collective magnetism. Although there are many amorphous magnets, most are ferromagnets with extensive site disorder, and the only structurally characterized example of an amorphous antiferromagnet is ionic FeF_3[39]. Thus, achieving a molecular amorphous antiferromagnet would allow for a chemical versatility inaccessible with metallic systems[40], as demonstrated herein. Direct synthesis of MOF glasses thus not only expands the range of feasible materials, but also the range of functional properties that can be achieved in MOF glasses, as demonstrated with the realization of MOF-supported photodetectors and topologically amorphous antiferromagnets.

Results

Direct synthesis of ZIFs glasses

Heating at 300 °C for 6 h a combination of ferrocene (0.16 mmol) and a mixture of imidazole:benzimidazole (0.32 mmol), sealed under vacuum, results in the formation of an orange transparent glassy monolith of formula $Fe(im)_{2-x}(bim)_x$, denoted as **dg-MUV-29** (dg = direct-glass), which can be prepared with different amounts of imidazole and benzimidazole ($x = 0.2$, 0.4, 0.5, and 0.6) (more details are in the SI). Note that this route produces polymeric cyclopentadiene as a byproduct.The amount of each ligand incorporated into the framework was determined by ^{1}H NMR spectroscopy (Table S1). Larger amounts of benzimidazole ($x \geq 0.78$) yield a new crystalline phase as a byproduct, denoted **MUV-28**, of formula $Fe(im)_1(bim)_1$, whereas the absence of benzimidazole ($x = 0$) produces the known crystalline **MUV-24(coi)**[25] (Fig. 1 and Figures S7–S9). Interestingly, reaction at lower temperature (150 °C) yields mixtures of crystalline phases which have been identified as **MUV-1**[36], **MUV-28** or **IMIDFE**[34].

No detectable Bragg diffraction peaks are observed in the different materials of the **dg-MUV-29** family, consistent with a glassy phase. A similar trend has been recently reported using an alloy of two different meltable coordination polymers instead of two different linkers, and depending on the amount of seeding the recrystallization process can be prevented[41]. Furthermore, differential scanning calorimetry (DSC) measurements exhibit no endothermic signal related to

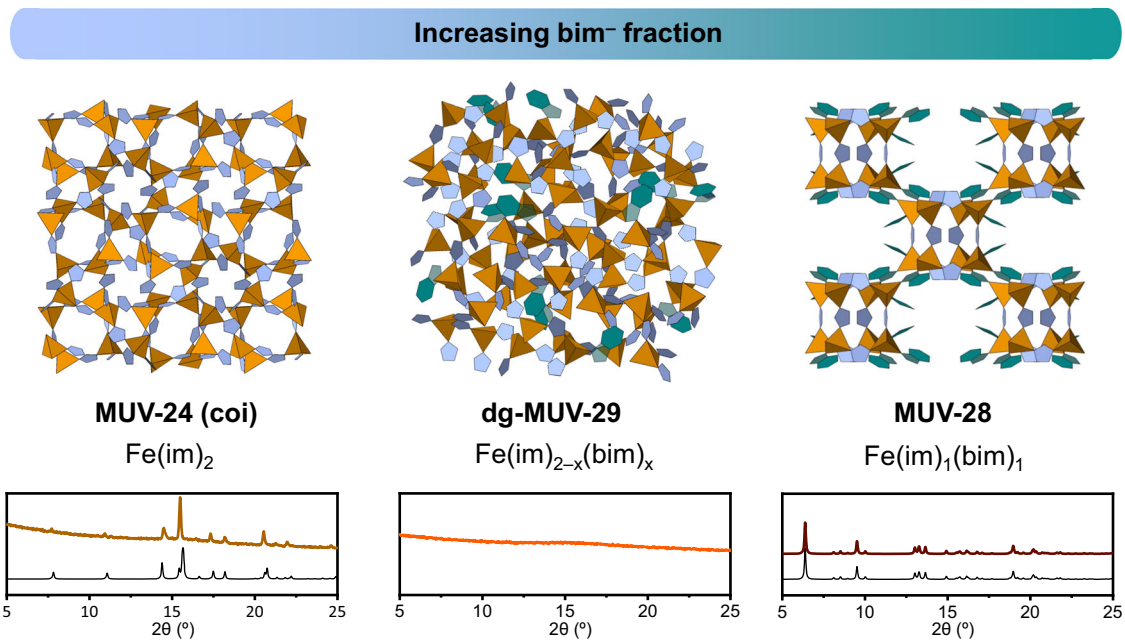

Fig. 1 | Structural analysis of compounds synthesized with varying imidazole:benzimidazole ratios. Schematic representation of the structures obtained under high temperature synthetic conditions (300 °C for 6 h) for **MUV-24(coi), dg-MUV-29**, and **MUV-28**. In the diagram, tetrahedral Fe^{II} centers are illustrated as orange tetrahedra. The imidazolate ligands are shown in light blue, and the benzimidazolate ligands in aquamarine blue. The corresponding powder X-ray diffraction pattern for each material is presented at the bottom, together with the calculated patterns of the crystalline materials. Note that the structure of **dg-MUV-29** was arbitrarily created to illustrate the lack of order. Source data are provided as a Source Data file.

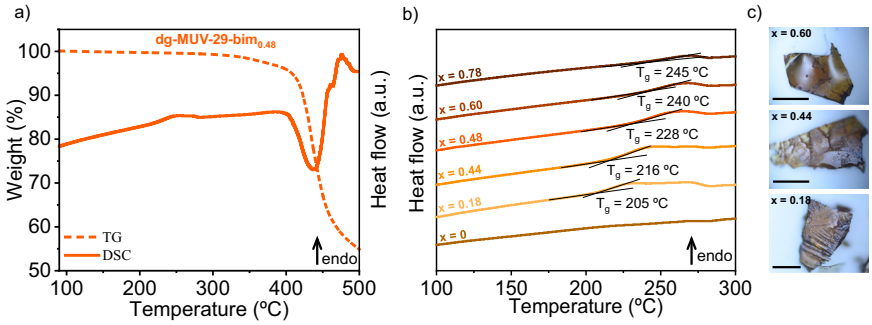

Fig. 2 | Thermal properties of ZIF-derived glasses. a Thermogravimetric analysis (TGA) and differential scanning calorimetry (DSC) curves of **dg-MUV-29-bim$_{0.48}$** **b** DSC of the materials obtained via high-temperature synthesis with variable im$^-$ to bim$^-$ ratios. **c** Optical images of various members of **dg-MUV-29**. Optical scale bars are 100 µm. Source data are provided as a Source Data file.

framework melting, but instead display the distinctive glass transition corresponding to their glassy nature (Fig. 2a). The glass transition temperature (T_g), defined as the peak onset temperature of the endothermic calorimetric signal of the glasses, ranges from 205 °C to 245 °C (Fig. 2b) depending on the incorporated amount of benzimidazole (x), and is slightly higher than for MQ **a$_g$-MUV-24**[25] (T_g = 190 °C), of formula Fe(im)$_2$. This effect is consistent with previous observations for the Zn analog, where T_g also increases with bim$^-$ concentration[42]. In all cases, an initial heating cycle up to 200 °C was performed to eliminate factors that could obscure the clear observation of the T_g, such as possible organic impurities or the sample-compartment effect, which might make the first scan particularly challenging. Upon further heating, the **dg-MUV-29** decomposes at a temperature of 450 °C.

The lack of long-range order in the glasses is confirmed by the absence of sharp features in their X-ray total scattering data. Pair distribution functions (PDF or $D(r)$) for **dg-MUV-29** were extracted from the total scattering data via appropriate corrections and subsequent Fourier transformation and are presented in Fig. 3a. Comparison of these data with crystalline Fe$_3$(im)$_6$(Him)$_2$ and MQ **a$_g$-MUV-24** shows that the short-range correlations are similar, although a new peak (peak "C" at 2.44 Å in Fig. 3a) can be detected in the **dg-MUV-29** family, corresponding to the distance between carbon atoms in the benzene ring of the benzimidazole ligand (Fig. 3b). The relative intensity of this peak increases as the amount of bim increases, confirming the successful incorporation of bim rings. The PDF peaks extend up to approximately 6 Å, which matches with the distance between neighboring Fe^{II} centers (5.8 – 6.1 Å in the crystalline phase **MUV-24**)[25]. This clearly indicates that the tetrahedral coordination of the Fe^{II} centers with imidazolate linkers is maintained in **dg-MUV-29** materials, and that their chemical environment is similar to that of MQ **a$_g$-MUV-24**. Importantly, the Bragg peaks attributed to crystalline impurities of Al and Fe$_2$N observed in the MQ **a$_g$-MUV-24**[25] data at higher Q values are absent in **dg-MUV-29** (Figure S13). These impurities prevented the study of the magnetic properties of **a$_g$-MUV-24**. In contrast, the direct-glass synthesis avoids the melting process required in the melt-quenched protocol, thereby preventing typical degradation and partial oxidation observed in MQ **a$_g$-MUV-24**[25]. The phase purity is unequivocally confirmed by Mössbauer spectroscopy, which is extremely sensitive to the geometry and oxidation state of iron centers. The characterization of the local environment of the metal ion in amorphous phases is very challenging due to the limited number of available techniques. Specific techniques such as ^{67}Zn NMR has greatly advanced the understanding of Zn^{II} centers within a random network, detecting short-range disorder in Zn-based amorphous glass ZIFs (a$_g$-ZIFs), which has been a significant achievement in the field[37]. The incorporation of Fe^{II} centers permits the possibility of using Mössbauer spectroscopy to study for the first time the local environment of a glassy phase. The Mössbauer spectra of **dg-MUV-29** measured at 80 K reveals two broad peaks with the same relative area but different widths (Fig. 3c). This is typical of amorphous materials where the Fe^{II} centers have the same coordination number but are located on sites with slightly different geometries and environments, leading to slightly different isomer shift (IS) and quadrupole splitting (QS)[43]. The spectrum can be fitted with a distribution of QS, and the average IS is consistent with tetrahedral coordination of all Fe^{II} cations as in MQ **a$_g$-MUV-24**[25]. The fitting procedure with this model was tested by calculating χ^2. For all spectra, calculated χ^2 values are between 1.2 and 1.5, close to 1, indicating that the deviations between the estimated and observed number of counts are mainly due to statistical error. Additionally, Mössbauer spectroscopy make it possible to monitor the oxidation state of the iron centers over time, revealing a 20 % oxidation after 24 h of air exposure (Figure S21).

Chemical diversity

The versatility of the direct-glass synthesis also provides the flexibility to incorporate linkers with diverse functionalities into the glassy phase. Until now, incorporating bulky benzimidazolate ligands with iron derivatives has been impossible because access to the ***cag*** topology is required, and that phase has remained elusive. Using the direct-glass synthesis, various analogs have been successfully prepared, denoted **dg-MUV-29-X**, where X is a different substituent in the position 5 of the benzimidazole ligand (X = NH$_2$, CH$_3$, Br, and Cl).

For the synthesis of **dg-MUV-29-X**, ferrocene (28 mg, 0.15 mmol) was combined with imidazole (Him) (15.3 mg, 0.23 mmol) and a 5-X-benzimidazole (0.07 mmol) and sealed under vacuum in a 4 mm diameter layering tube. The mixtures were heated at 300 °C for 6 h, producing an orange glass in each case corresponding to **dg-MUV-29-NH$_2$**, **dg-MUV-29-CH$_3$**, **dg-MUV-29-Br**, and **dg-MUV-29-Cl**, similar in appearance to **dg-MUV-29** (Fig. 4a). The same synthetic fraction was maintained in all cases, with $x \approx 0.5$. The incorporated amount of each ligand into the framework was determined by ^{1}H NMR spectroscopy (Table S4 and Section S3.3) and closely matches the synthetic amount. The amount of incorporated Xbim can be varied in a controlled manner by adjusting the ratio of the reactants. The incorporation of the different benzimidazolate ligands into the glassy material can be clearly followed for **dg-MUV-29-Cl** and **dg-MUV-29-Br** using EDX-SEM, showing that Cl and Br are uniformly distributed throughout the monolithic framework (Fig. S47-S48). PXRD measurements of the resultant monolithic phases revealed the absence of any Bragg diffraction for all analogs (Fig. 4b).

DSC measurements of the different analogs of the **dg-MUV-29-X** family reveals the absence of endothermic peaks corresponding to framework melting but instead show the characteristic T_g of the glassy nature of the material (Fig. 4c). The glass transition is nearly identical across the samples, and reversible, allowing for multiple cycles without any alteration, as also observed in **dg-MUV-29** (Fig. S44-S45). The

https://doi.org/10.1038/s41467-025-63837-w

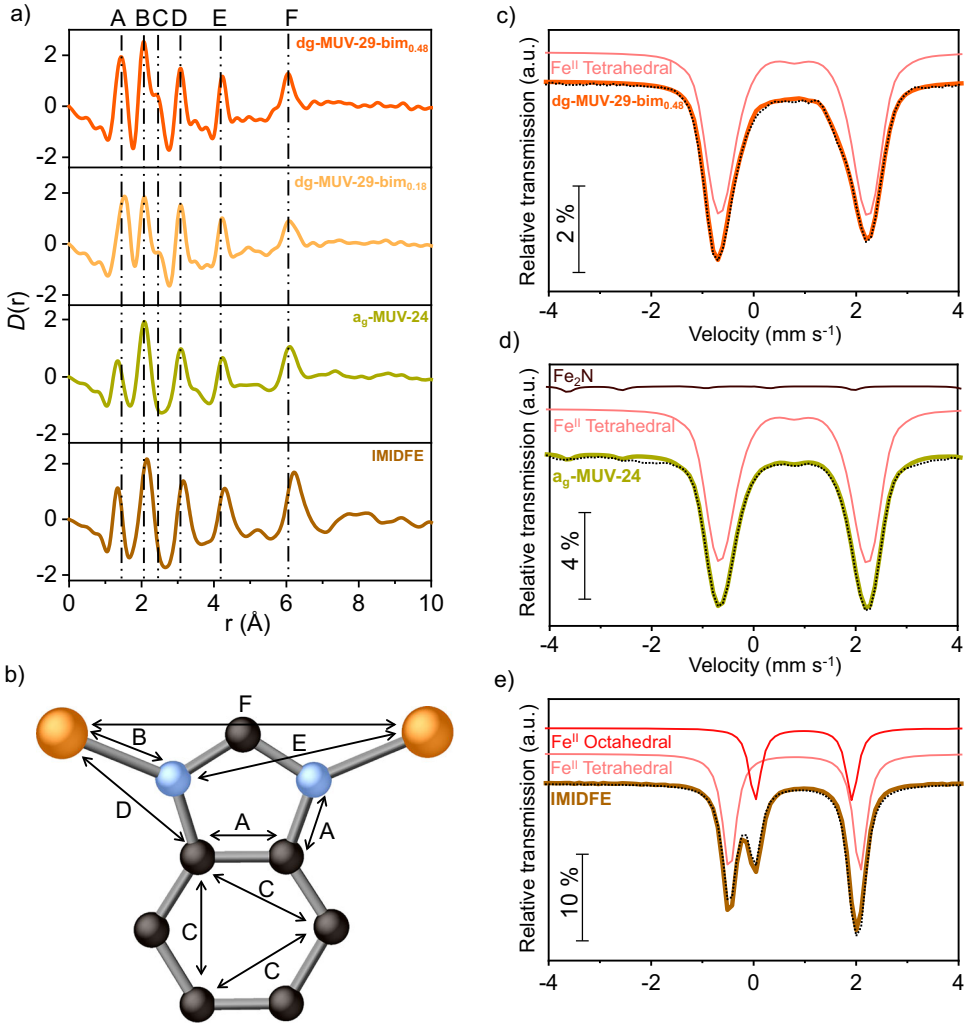

Fig. 3 | Structural characterization of modified ZIF-derived glasses using pair distribution function (PDF) analysis and Mössbauer spectroscopy. a X-ray PDF in the form of D(r) of **dg-MUV-29-bim$_{0.48}$**, **dg-MUV-29-bim$_{0.18}$**, **a$_g$-MUV-24** and **IMIDFE**. **b** Schematic representation of the benzimidazolate bridge coordinated to two Fe^{II} centers and the connectivity between tetrahedral Fe^{II} ions with benzimidazolate linkers. Orange spheres represent Fe atoms, blue spheres represent nitrogen atoms, and black spheres represent carbon atoms. Hydrogen atoms have been omitted for clarity. Mössbauer spectra of **dg-MUV-29-bim$_{0.48}$** (**c**) **a$_g$-MUV-24** (**d**) and **IMIDFE** (**e**) samples, displayed with lines overlaid on the experimental data. These lines represent the sum of doublets and sextets, or distributions of quadrupole splitting (QS) (see Table S2), and are slightly shifted for clarity. Source data are provided as a Source Data file.

possibility of incorporating bulkier ligands into the iron framework allows further tunability of the system and has an effect on the CO_2 gas sorption capability of the glasses (Fig. S49).

Topologically disordered amorphous antiferromagnets

Based on the combined results of all the characterization techniques, we can conclude that the direct-glass synthesis method enables the production of a high-purity Fe^{II} phase, which cannot be achieved through conventional melt-quenching methods. This level of purity allows for precise measurement of magnetic correlations of the first phase-pure MOF glass containing paramagnetic ions, providing insight into the nature of the magnetic phase of **dg-MUV-29**. Bulk magnetic measurements confirmed antiferromagnetic interactions typical of Fe^{II} imidazolate MOFs[44] (Fig. 5a), as indicated by Curie-Weiss fitting (T_{CW} = −24.7(4) K, implying J = 16.5(3) K with a moment slightly larger than the spin-only value for high-spin tetrahedral FeII (C = 4.19(1) emu mol^{-1} K, equivalent to g = 2.36)[45]. Unlike crystalline iron imidazolates, no clear ordering transition at higher temperatures was observed in static susceptibility measurements, confirming the phase purity. AC susceptibility measurements (Fig. 5b) revealed a clear cusp at 5.2(2) K, consistent with the presence of cooperative magnetic interactions. The magnetization as a function of the field was linear, indicating moderately strong antiferromagnetic interactions with no ferromagnetic components (Fig. S22).

The Mössbauer spectrum of **dg-MUV-29** at 4 K shows magnetic hyperfine splitting (Fig. 5c), revealing strong magnetic correlations consistent with the transition observed in the magnetization data. The magnetic hyperfine interactions were found to be complex, requiring detailed modeling of the hyperfine interaction parameters, including the quadrupole interaction (Δ = −2.42 mm s^{-1}), asymmetry parameter (η = 0.70), and magnetic hyperfine field (B_{hf} = 15 T). These parameters suggest significant orbital magnetic momentum and confirm the high-spin Fe^{II} state (Fig. 5c). These findings support the hypothesis that **dg-MUV-29** is a continuous random network (CRN) antiferromagnet, which would be a new type of magnetic phase. These materials exhibit a completely disordered long-range structure while maintaining a strong degree of local uniformity. This implies that exchange disorder, i.e., variations in the strength and sign of magnetic interactions, are small, and hence the inherent topological amorphousness of the network is driving the observed magnetic properties. Although there are many amorphous ferromagnets, amorphous antiferromagnets are extremely rare. To further investigate this hypothesis, we conducted

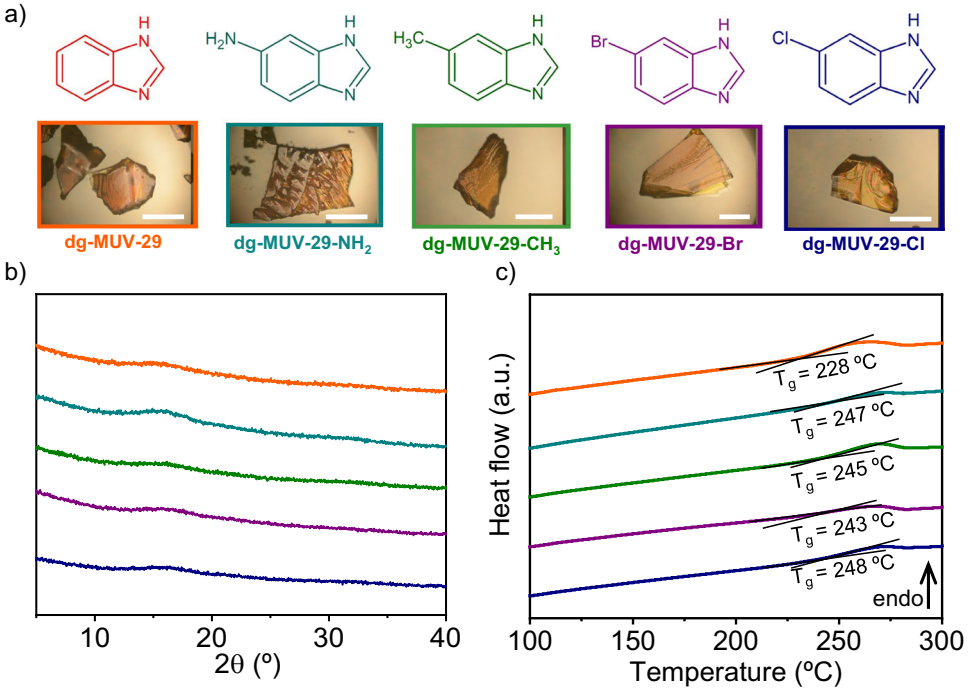

Fig. 4 | Structural analysis of compounds synthesized with different benzimidazole derivatives. a Optical images of different **dg-MUV-29-X** monolithic glass. Scale bars are 100 µm. **b** X-ray powder diffractograms of **dg-MUV-29-X**. **c** Differential scanning calorimetry (DSC) first upscan of **dg-MUV-29-X** family. To calculate the T_g onset, the material was heated to 200 °C to avoid process that could obscure the T_g. Source data are provided as a Source Data file.

semi-classical Monte Carlo simulations using the well-studied Wooten-Winer-Weaire CRN model of amorphous silicon[46], simulating a 512-spin periodic approximant of the tetrahedral continuous random network (Section S2.9). We note that different materials with tetrahedral CRN structures, though sharing family relationships, are likely to have distinct topological features (e.g., ring statistics), that could play a role in their magnetic function, and so improved structural models will no doubt shed further light on their behavior[47]. The simulated susceptibility was in quantitative agreement with experimental data, particularly at high temperatures. Below $T_c = 13$ K, the simulated susceptibility showed a cusp and deviation consistent with a long-range ordering transition, at a temperature which mirrors that of analogous crystalline systems, but higher than observed for **dg-MUV-29**.

To investigate the local spin correlations, we conducted powder neutron diffraction measurements using diffractometer D20 at the ILL on a deuterated sample across a broad temperature range (1.8 to 100 K) (Fig. 5d). Subtraction of the highest temperature data (100 K) revealed short-range magnetic correlations with a distinct broad peak at 0.79 $Å^{-1}$. This peak is lower than the first sharp diffraction peak from structural diffraction, and occurs at a similar Q to the crystalline antiferromagnet analogs[36], suggestive of antiferromagnetic spin-spin correlations with a correlation length similar to the structure itself. Comparison of the experimental neutron diffraction data with our Monte Carlo simulations, using the metal-metal distance determined from PDF measurements, $r_0 = 6.20$ Å, showed qualitative agreement, particularly from simulations near the ordering transition of the Monte Carlo simulations at $T_c = 13$ K. However, we note that deviations between experiment and simulation at low temperatures highlight the challenges of modeling amorphous materials, in particular the finite size of our periodic approximant and complexities beyond the minimal model of nearest-neighbor antiferromagnetism (Section S2.11). Our Monte Carlo simulation shows spin and quadrupole correlations indicating a speromagnetic state (Figs. 5e and S32), characterized by a disordered arrangement of magnetic moments (spins) on a local scale, while still maintaining no net magnetization across the entire system[48].

The combined results from neutron scattering and magnetometry strongly indicate that this material behaves as an amorphous antiferromagnet with a continuous random network structure and predominantly nearest-neighbor Heisenberg interactions. The reported magnetic **dg-MUV-29** family is an unusual kind of amorphous magnet, where local exchange and single-ion anisotropy disorder is expected to be small, meaning the intrinsic topological disorder dominates their properties. Unlike previous amorphous antiferromagnets[43], this material exhibits minimal exchange disorder because each Fe ion has a similar local environment with four nearest neighbors, and Fe is the sole framework-forming cation[49,50]. This contrasts with amorphous metals, which typically exhibit significant exchange and site disorder[40].

Scalability and processability

The ability to bypass the melting process and eliminate the need for a crystalline intermediate enables easier scalability compared to the conventional melt-quenching approach. In melt-quenching, a monolith forms by fusing individual crystals upon reaching the liquid state. In contrast, this method allows the amorphous material to directly form during synthesis, increasing its uniformity. This enables the production of large quantities of glass in film form simply by increasing the size of the layering tube used as a reactor. To demonstrate the scalability and processability of **dg-MUV-29**, we have used it as a substrate for a centimeter-scale thin-film photodetector based on methylammonium lead iodide ($MAPbI_3$), replacing the conventional glass typically used. $MAPbI_3$ is an archetypal material within the broader metal halide perovskite family, a class of semiconductor with promising applications in optoelectronic devices such as photodetectors, among others[51]. MOFs have been used in combination with perovskites as additives (blended with the active material), host materials, or functional layers in order to improve the device performances[17,52–54], but their use as substrates in optoelectronic devices remains elusive, as producing large-area homogenous and monolithic MOFs is challenging. As most perovskite optoelectronic devices are fabricated on soda-lime glass, **dg-MUV-29** is used here as

https://doi.org/10.1038/s41467-025-63837-w

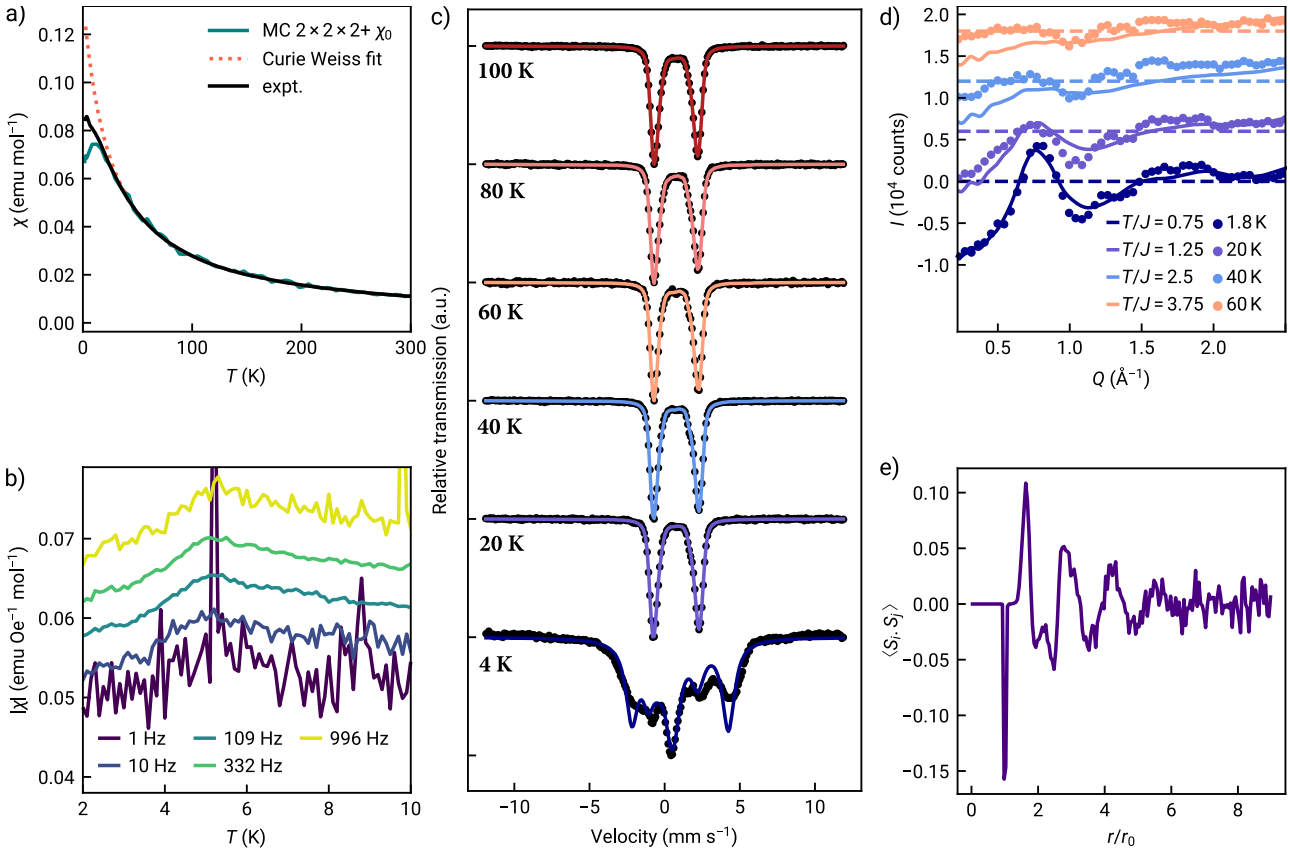

Fig. 5 | Magnetic properties of ZIF-derived glasses. a Thermal dependence of magnetic susceptibility in the temperature range 2–300 K of **dg-MUV-29**. The experimental data (expt., black line) have been fitted (red dotted line) following the Curie-Weiss model. **b** Temperature dependence of the a.c. susceptibility of **dg-MUV-29** measured at different frequencies. **c** Mössbauer measurements at different temperatures of **dg-MUV-29**. The lines over the experimental points are the estimated distributions of quadrupole splittings (QS). **d** *I*(*Q*) data, offset by 5000; dots represent the experimental data of **dg-MUV-29**, and the line represents the Monte Carlo (MC) simulation. The MC simulation is matched to temperature, with 1.8 K data plotted against 13 K. An empirical scale, offset, and linear background have been applied to all MC data, fixed to the lowest temperature, and distances are scaled by the experimentally determined metal-metal distance $r_0 = 6.20$ Å. **e** Real space spin correlation function derived from MC simulations showing antiferromagnetic alternation that decays with increasing distance, *r*
Source data are provided as a Source Data file.

the substrate for a simple proof-of-concept lateral perovskite photodetector. After isolating a centimeter-size monolithic **dg-MUV-29** (see Fig. S35), we used vacuum deposition[55,56] to process the perovskite on top of the glass by co-sublimation of PbI_2 and MAI, followed by evaporation of gold contacts through a shadow mask (Fig. 6a, b). As shown in Fig. S38, the diffraction pattern and absorption profile confirm the formation of $MAPbI_3$ on **dg-MUV-29**. The current of the resulting **dg-MUV-29**/perovskite photodetector was measured as a function of the applied field under illumination (white light, 100 mW·cm^{-2}) and in the dark, as shown in Fig. 6c. The device showed the expected photoconductive behavior, with the current increasing more than three orders of magnitude upon illumination, with an on/off ratio > 1000 at 0.4 V/µm. Note that the variation between several devices is minor, indicating a good reproducibility of the detector fabricated on **dg-MUV-29**. The on-current was found to be also stable for several consecutive measurements (Fig. 6d), which indicates an overall good quality of the $MAPbI_3$ film grown on the **dg-MUV-29** substrate, as well as the mechanical stability of the MOF itself. Only a minor difference is observed between devices deposited on commercial float glass and the **dg-MUV-29** (Fig. S37), likely arising from the different optical quality of the two materials.

Discussion

The solvent-free methodology presented here facilitates the direct synthesis of a previously unreported family of MOF-derived glasses, designated **dg-MUV-29**, eliminating the necessity for a pre-existing crystalline phase. This innovative approach yields high-purity Fe^{II} glasses while effectively mitigating the oxidation and degradation issues commonly associated with traditional melt-quenching techniques. In this work, we have aimed to demonstrate a comprehensive research approach involving three key aspects, where direct synthesis has played a pivotal role in advancing various areas. Firstly, the versatility of this synthetic technique allows for the incorporation of a diverse array of ligands featuring varying functional groups, leading to the development of the expanded **dg-MUV-29-X** family. Such adaptability broadens the scope of potential applications and avenues for future research involving these materials. Secondly, we have shown that the resulting free-standing films of glassy MOFs can be used as substrates for device integration, and have demonstrated this applicability with the preparation of a photodevice using **dg-MUV-29** as a substrate. Finally, this methodology establishes a robust platform for probing the magnetic properties of molecular-based random networks, thereby enhancing our understanding of the magnetism inherent in disordered systems. In summary, this direct-glass synthesis method proves to be a highly effective strategy for advancing the development of glassy ZIFs, thus paving the way for new research initiatives and applications. The implications of glassy ZIFs in the study of disordered systems underscore their potential to significantly impact the field of materials science.

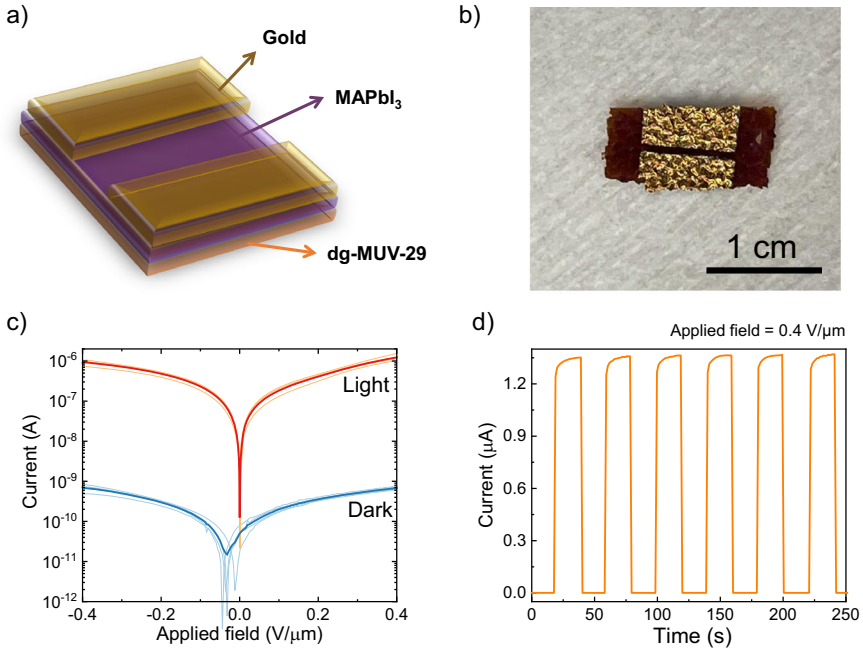

Fig. 6 | Perovskite photodetector fabricated on a ZIF-derived glass substrate. **a** Schematics and **b** photograph of the perovskite photodetector prepared on the **dg-MUV-29** substrate. **c** Current vs. applied field for perovskite detectors on **dg-MUV-29**, recorded under illumination (orange) and in the dark (light blue). The thick red and blue curves are the mathematical average of the corresponding curves recorded under illumination and in the dark, respectively. **d** Current response of the device at an applied field of 0.4 V/μm when exposed to consecutive light pulses. Source data are provided as a Source Data file.

Methods

Synthesis

Ferrocene (0.15 mmol) was combined with a mixture of imidazole (Him) (range: 0.18–0.30 mmol) and benzimidazole (Hbim) (range: 0–0.12 mmol) or 5-X-benzimidazole (0.07 mmol), maintaining a total ligand amount of 0.30 mmol. The mixture was subjected to at least three Ar–vacuum cycles to remove moisture and oxygen, then sealed under vacuum in a 4 mm diameter layering tube. It was heated at 300 °C for 6 h, producing an orange glass. After cooling to room temperature, the tube was opened and unreacted precursors were removed using acetonitrile. Although the resulting materials remain stable in air for several hours and oxidize only slowly, sensitive measurements—such as neutron diffraction and Mössbauer spectroscopy—are carried out under strict inert atmosphere conditions to prevent any risk of oxidation.

X-ray powder diffraction

The samples were lightly ground in an agate mortar and pestle and used to fill 0.7 mm borosilicate capillaries that were mounted and aligned on a Bruker D8 Discover powder diffractometer, using Cu K_α radiation (λ = 1.54056 Å). The detector was an EIGER2 R 500 K, multimode 2D.

Differential scanning calorimetry

Differential scanning calorimetry (DSC) measurements were conducted using a TRIOS DSC 250 instrument. Activated samples (10–15 mg) were placed in an aluminum crucible (30 μL) with a pierced lid. All the measurements were performed under a continuous N_2 flow of 50 ml min^{-1}. The sample was initially heated to 40 °C, followed by a 15-minute isotherm to stabilize the environment. Subsequently, the sample was heated at a rate of 10 °C min^{-1}. Upon reaching the final temperature, a 10-minute isotherm was performed to ensure a complete phase change. The sample was then cooled back at 10 °C min^{-1}. It is important to note that DSC results are highly dependent on the experimental conditions. Therefore, when changing the equipment, parameters such as N_2 flow, sample amount, or size of the hole in the crucible lid (prepared using a standard needle of approximately 0.6 mm diameter) may need to be adjusted to accurately observe the phase changes.

Thermogravimetric analysis

Thermogravimetric analysis (TGA) measurements were conducted using a TGA 550 instrument (TA Instruments). All the samples were loaded in a platinum pan, under air or N_2 atmosphere. Initially, the sample was heated to 40 °C and held isothermally for 15 min to stabilize. Subsequently, the sample was heated at a rate of 10 °C min^{-1}.

Mössbauer Spectroscopy

Mössbauer spectra were collected in transmission mode using a conventional constant-acceleration spectrometer from Wissel (Starnberg, Germany) and a 50 mCi ^{57}Co source in a Rh matrix. The velocity scale was calibrated using α-Fe foil. Isomer shifts, IS, are given relative to this standard at room temperature. The absorbers were obtained by gently packing the samples into Perspex holders. Absorber thicknesses were calculated on the basis of the corresponding electronic mass-absorption coefficients for the 14.4 keV radiation[57]. The low temperature measurements at 4 K and above were performed with the sample in liquid He and in He exchange gas, respectively, in a Janis (Westerville, OH, USA) bath cryostat, model SVT-400. The spectra were fitted to Lorentzian lines using a non-linear least-squares method[58]. Line widths and relative areas of both peaks in each doublet were kept equal during the refinement. Distributions of quadrupole splittings were fitted according to the histogram method[59].

X-ray total scattering

Neutron total scattering data were collected at room temperature using a PANalytical Empyrean laboratory diffractometer, equipped with an Ag-K_α source and focusing mirrors. The samples were placed in 1 mm diameter quartz glass capillaries. Each sample underwent multiple scans, with a cumulative data collection time exceeding 24 h per sample. Additionally, measurements were conducted on an empty

capillary and the diffractometer background. The resulting X-ray total scattering patterns were processed using the GudrunX[60] program to produce a normalized Pair Distribution Function (PDF), optimized to ensure, for example, that the low-r portion of $g(r)$ oscillates around −1. The total scattering structure factor, $S(Q)$, was Fourier transformed for $0.6 < Q < 18.5$ Å^{-1} to obtain the PDF.

Neutron total scattering

X-ray total scattering data were collected at temperatures of 5 K (base), 10 K, 15 K (just above the transition), 30 K, 60 K, and 120 K. Each temperature required a collection time of at least 3 h per sample. The sample was measured using the ILL D20 instrument at a wavelength of 2.41 Å. The sample was predominantly deuterated, achieved by using deuterated imidazole (Dim, $C_3N_2D_4$) and deuterated ferrocene [$Fe(C_5D_5)_2$], with a minor hydrogen presence from benzimidazole (Hbim).

Magnetic susceptibility (SQUID)

Magnetic susceptibility measurements were conducted on powdered samples (5–20 mg) using a SQUID magnetometer (Quantum Design MPMS-XL-5 and MPMS-XL-7). Variable-temperature (2–300 K) direct current (d.c.) magnetic susceptibility measurements were performed in applied fields of 1.0 kOe, along with variable field magnetization measurements up to ±5 T at 2.0 K. Additionally, variable-temperature (2–10 K) alternating current (a.c.) magnetic susceptibility measurements were conducted in a ± 4.0 G oscillating field at frequencies ranging from 1 to 996 Hz, under a zero d.c. field.

Photodetector fabrication

CH_3NH_3I (MAI) and PbI_2 were purchased from Luminescence Technology Corp. All materials were used as received. For $MAPbI_3$ deposition, MAI and PbI_2 precursors were simultaneously evaporated using the following process. The evaporation chamber employed has only two quartz crystal microbalances (QCMs), one close to the PbI_2 source designated to monitor exclusively the PbI_2 precursor (PbI_2-QCM), with no cross reading, and a second one fixed at the height of the substrates to monitor simultaneously the total amount of PbI_2 and MAI mass reaching the substrates ($MAPbI_3$-QCM). Initially, only PbI_2 is heated, and the temperature is fine tuned to lead to a stable sublimation rate of precisely 0.50 Å s^{-1} on both PbI_2-QCM and $MAPbI_3$-QCM. Then, MAI is heated, and the temperature adjusted so that the sublimation detected on the $MAPbI_3$-QCM increases from the previous 0.50 Å s^{-1} to 0.66 Å s^{-1}, while the rate on the PbI_2-QCM is kept stable at 0.50 Å s^{-1}. During the evaporation the pressure of the chamber was maintained at $5{\cdot}10^{-6}$ mbar. Gold contact were evaporated in another vacuum chamber through a shadow mask, defining lateral electrodes with channel length of 500 μm and width of 500 mm. The devices were encapsulated with Al_2O_3 (30 nm), deposited by atomic layer deposition in a Arradiance reactor at 40 °C[52].

Data availability

All data generated and analyzed during this study are included in this Article and its Supplementary Information and have been deposited in the Zenodo open repository (https://doi.org/10.5281/zenodo.16747533). Atomic coordinates and structure factors for the reported crystal structure has been deposited in the Cambridge Crystallographic Data Centre under the accession code CCDC 2416331 (**MUV-28**). Copies of the data can be obtained free of charge from www.ccdc.cam.ac.uk/structures/. Neutron scattering data obtained at D20 instrument are available at https://doi.org/10.5291/ILL-DATA.5-32-950 Source data are provided with this paper.

Code availability

Complete Python scripts for this fitting procedure are included in the deposited data (https://doi.org/10.17639/nott.7549).

References

1. Greaves, G. N. & Sen, S. Inorganic glasses, glass-forming liquids and amorphizing solids. *Adv. Phys.* **56**, 1–166 (2007).
2. Wang, W. H. Bulk metallic glasses with functional physical properties. *Adv. Mater.* **21**, 4524–4544 (2009).
3. Ma, N. & Horike, S. Metal–organic network-forming glasses. *Chem. Rev.* **122**, 4163–4203 (2022).
4. Wang, M. et al. Functions and applications of emerging metal–organic-framework liquids and glasses. *Chem. Commun.* **59**, 7126–7140 (2023).
5. Bennett, T. D. et al. Looking into the future of hybrid glasses. *Nat. Chem.* **16**, 1755–1766 (2024).
6. Furukawa, H., Cordova, K. E., O'Keeffe, M. & Yaghi, O. M. The chemistry and applications of metal–organic frameworks. *Science* **341**, 1230444 (2013).
7. Krause, S., Hosono, N. & Kitagawa, S. Chemistry of soft porous crystals: structural dynamics and gas adsorption properties. *Angew. Chem. Int. Ed.* **59**, 15325–15341 (2020).
8. Maurin, G., Serre, C., Cooper, A. & Férey, G. The new age of MOFs and of their porous-related solids. *Chem. Soc. Rev.* **46**, 3104–3107 (2017).
9. Qiao, A. et al. A metal–organic framework with ultrahigh glass-forming ability. *Sci. Adv.* **4**, eaao6827 (2018).
10. Fonseca, J., Gong, T., Jiao, L. & Jiang, H. L. Metal–organic frameworks beyond crystallinity: amorphous MOFs, MOF liquids and MOF glasses. *J. Mater. Chem. A* **9**, 10562–10611 (2021).
11. Frentzel-Beyme, L., Kolodzeiski, P., Weiß, J. B., Schneemann, A. & Henke, S. Quantification of gas-accessible microporosity in metal–organic framework glasses. *Nat. Commun.* **13**, 7750 (2022).
12. Zhou, C. et al. Metal–organic framework glasses with permanent accessible porosity. *Nat. Commun.* **9**, 5042 (2018).
13. Wang, Y. et al. A MOF glass membrane for gas separation. *Angew. Chem. Int. Ed.* **59**, 4365–4369 (2020).
14. Yang, Z. et al. ZIF-62 glass foam self-supported membranes to address CH4/N2 separations. *Nat. Mater.* **22**, 888–894 (2023).
15. Lin, R. et al. Mechanochemically synthesised flexible electrodes based on bimetallic metal–organic framework glasses for the oxygen evolution reaction. *Angew. Chem. Int. Ed.* **61**, e202112880 (2022).
16. Gao, C. et al. Metal–organic framework glass anode with an exceptional cycling-induced capacity enhancement for lithium-ion batteries. *Adv. Mater.* **34**, 2110048 (2022).
17. Hou, J. et al. Liquid-phase sintering of lead halide perovskites and metal–organic framework glasses. *Science* **374**, 621–625 (2021).
18. Yu, Z., Tang, L., Ma, N., Horike, S. & Chen, W. Recent progress of amorphous and glassy coordination polymers. *Coord. Chem. Rev.* **469**, 214646 (2022).
19. Bennett, T. D. et al. Hybrid glasses from strong and fragile metal–organic framework liquids. *Nat. Commun.* **6**, 8079 (2015).
20. Zheng, Z., Rong, Z., Nguyen, H. L. & Yaghi, O. M. Structural chemistry of zeolitic imidazolate frameworks. *Inorg. Chem.* **62**, 20861–20873 (2023).
21. Tao, H., Bennett, T. D. & Yue, Y. Melt-quenched hybrid glasses from metal–organic frameworks. *Adv. Mater.* **29**, 1601705 (2017).
22. Gaillac, R. et al. Liquid metal–organic frameworks. *Nat. Mater.* **16**, 1149–1155 (2017).
23. Bennett, T. D. et al. Melt-quenched glasses of metal–organic frameworks. *J. Am. Chem. Soc.* **138**, 3484–3492 (2016).
24. Frentzel-Beyme, L. et al. Meltable mixed-linker zeolitic imidazolate frameworks and their microporous glasses: from melting point engineering to selective hydrocarbon sorption. *J. Am. Chem. Soc.* **141**, 12362–12371 (2019).
25. León-Alcaide, L. et al. Meltable, glass-forming, iron zeolitic imidazolate frameworks. *J. Am. Chem. Soc.* **145**, 11258–11264 (2023).

26. Hou, J. et al. Halogenated metal–organic framework glasses and liquids. *J. Am. Chem. Soc.* **142**, 3880–3890 (2020).
27. Song, J. et al. Modulating liquid–liquid transitions and glass formation in zeolitic imidazolate frameworks by decoration with electron-withdrawing cyano groups. *J. Am. Chem. Soc.* **145**, 9273–9284 (2023).
28. Frentzel-Beyme, L. et al. Porous purple glass – a cobalt imidazolate glass with accessible porosity from a meltable cobalt imidazolate framework. *J. Mater. Chem. A* **7**, 985–990 (2019).
29. León-Alcaide, L. et al. Solvent-free approach for the synthesis of heterometallic Fe–Zn ZIF glass via a melt-quenched process. *Chem. Sci.* **16**, 7956–7955 (2025).
30. Stepniewska, M., Østergaard, M. B., Zhou, C. & Yue, Y. Towards large-size bulk ZIF-62 glasses via optimizing the melting conditions. *J. Non-Cryst. Solids* **530**, 119806 (2020).
31. Smirnova, O. et al. Precise control over gas-transporting channels in zeolitic imidazolate framework glasses. *Nat. Mater.* **23**, 262–270 (2023).
32. Thorne, M. F. et al. Glassy behaviour of mechanically amorphised ZIF-62 isomorphs. *Chem. Commun.* **57**, 9272–9275 (2021).
33. Wei, Y.-S., Fan, Z., Luo, C. & Horike, S. Desolvation of metal complexes to construct metal–organic framework glasses. *Nat. Synth.* **3**, 214–223 (2024).
34. Rettig, S. J. et al. Transition metal azolates from metallocenes. 2. Synthesis, X-ray structure, and magnetic properties of a three-dimensional polymetallic iron(II) imidazolate complex, a low-temperature weak ferromagnet. *J. Am. Chem. Soc.* **119**, 8675–8680 (1997).
35. López-Cabrelles, J. et al. Solvent-free synthesis of ZIFs: a route toward the elusive Fe(II) analogue of ZIF-8. *J. Am. Chem. Soc.* **141**, 7173–7180 (2019).
36. López-Cabrelles, J. et al. Isoreticular two-dimensional magnetic coordination polymers prepared through pre-synthetic ligand functionalization. *Nat. Chem.* **10**, 1001–1007 (2018).
37. Madsen, R. S. K. et al. Ultrahigh-field 67Zn NMR reveals short-range disorder in zeolitic imidazolate framework glasses. *Science* **367**, 1473–1476 (2020).
38. Froufe-Pérez, L. S. et al. Role of short-range order and hyperuniformity in the formation of band gaps in disordered photonic materials. *Phys. Rev. Lett.* **117**, 053902 (2016).
39. Greneche, J. M. et al. Structural aspects of amorphous iron(III) fluorides. *J. Phys. C.* **21**, 1351 (1988).
40. Coey, J. M. D. Amorphous magnetic order. *J. Appl. Phys.* **49**, 1646–1652 (1978).
41. Watcharatpong, T. et al. Alloying one-dimensional coordination polymers to create ductile. *J. Am. Chem. Soc.* **146**, 23412–23416 (2024).
42. Yang, Y. et al. Prediction of the glass transition temperatures of zeolitic imidazolate glasses through topological constraint theory. *J. Phys. Chem. Lett.* **9**, 6985–6990 (2018).
43. Greneche, J. M. et al. Mössbauer study of an amorphous iron(III) fluoride: FeF_3, XHF ($0 \le x \le 1$). *Solid State Commun.* **63**, 435–438 (1987).
44. López-Cabrelles, J. et al. Chemical design and magnetic ordering in thin layers of 2D metal–organic frameworks. *J. Am. Chem. Soc.* **143**, 18502–18510 (2021).
45. Burbridge, C. D. & Goodgame, D. M. L. Electronic and Mössbauer spectra of some iron(II) halide hydrates. *J. Chem. Soc. A* **1410**, 1413 (1968).
46. Wooten, F., Winer, K. & Weaire, D. Computer generation of structural models of amorphous Si and Ge. *Phys. Rev. Lett.* **54**, 1392 (1985).
47. Nicholas, T. C. et al. The structure and topology of an amorphous metal–organic framework. *arXiv* https://doi.org/10.48550/arXiv.2503.24367 (2025).
48. Férey, G., Varret, F. & Coey, J. M. D. Amorphous FeF3: a non-crystalline magnet with antiferromagnetic interactions. *J. Phys. C.* **12**, L531 (1979).
49. Cliffe, M. et al. Structural simplicity as a restraint on the structure of amorphous silicon. *Phys. Rev. B* **95**, 224108 (2017).
50. Xie, R. et al. Hyperuniformity in amorphous silicon based on the measurement of the infinite-wavelength limit of the structure factor. *Proc. Natl. Acad. Sci. USA* **110**, 13250–13254 (2013).
51. Wang, H. & Kim, D. H. Perovskite-based photodetectors: materials and devices. *Chem. Soc. Rev.* **46**, 5204–5236 (2017).
52. Nevruzoglu, V. et al. Improving the stability of solar cells using metal–organic frameworks. *J. Mater. Chem. A* **4**, 7930–7935 (2016).
53. Li, X. et al. Interfacial alloying between lead halide perovskite crystals and hybrid glasses. *Nat. Commun.* **14**, 7612 (2023).
54. Tsai, H. et al. Bright and stable light-emitting diodes made with perovskite nanocrystals stabilized in metal–organic frameworks. *Nat. Photonics* **15**, 843–849 (2021).
55. Liu, M., Johnston, M. B. & Snaith, H. J. Efficient planar heterojunction perovskite solar cells by vapour deposition. *Nature* **501**, 395–398 (2013).
56. Zanoni, K. P. S. et al. Photovoltaic devices using sublimed methylammonium lead iodide perovskites: long-term reproducible processing. *Sol. RRL* **7**, 2201073 (2023).
57. Long, G. J., Cranshaw, T. E. & Longworth, G. The ideal Mössbauer effect absorber thicknesses. *Mössbauer Effect Ref. Data J.* **42**, 49 (1983).
58. Brand, R. A. *Normos Mössbauer fitting program v.90* (Wissel GMbH, Stanberg, 1994).
59. Hesse, J. & Rubartsch, A. Model independent evaluation of overlapped Mössbauer spectra. *J. Phys. E* **7**, 526 (1974).
60. Soper, A. GudrunN and GudrunX: programs for correcting raw neutron and X-ray diffraction data to differential scattering cross section. *Rutherford Appleton Lab. Tech. Rep.* (2011).

Acknowledgements

G.M.E. acknowledges support from the European Union (ERC-2016-CoG 724681-S-CAGE), grants PID2023-152920NB-I00, and María de Maeztu Centre of Excellence Programmes CEX2024-001467-M, funded by MCIN/AEI/10.13039/501100011033 and cofinanced by FEDER, and the Generalitat Valenciana (CIPROM/2022/48, and IDIFEDER2021/075). L.L.A. thanks MICIN for a pre-doctoral fellowship (PRE2019-089295). This study forms part of the Advanced Materials program and was supported by MCIN with funding from European Union NextGenerationEU (PRTR-C17.I1) and by Generalitat Valenciana (projects MFA/2022/31). We also thank the University of Valencia for research facilities (SCSIE). M.J.C. acknowledges UKRI funding (EP/X042782/1). J.C.W. and B.J.C.V. acknowledge FCT (Portugal) through contracts UID/Multi/04349/2019 and PTDC/QUI-QIN/32240/2017. M.S. acknowledges financial support from the Comunitat Valenciana (CISEJI/2022/43). We acknowledge the Institut Laue-Langevin for access to beamline D20. Dr J. A. M. Paddison is thanked for the use of his software for magnetic Monte Carlo simulations.

Author contributions

L.L.A. synthesized and characterized all the materials. L.M.G. and M.S. prepared and characterized the photodetector. B.J.C.V. and J.C.W. conducted and analyzed the Mössbauer measurements. J.A.R.V. and O.F. assisted with the performance and analysis of the neutron measurements. M.C. analyzed the magnetic behavior of the materials and performed the theoretical calculations. L.L.A. carried out the total scattering experiments under the supervision of D.A.K. G.M.E. conceived the idea and designed the experiments. L.L.A. and G.M.E. prepared the manuscript. All authors contributed to the preparation of the manuscript.

Competing interests
The authors declare no competing interests.

Additional information
Supplementary information The online version contains supplementary material available at https://doi.org/10.1038/s41467-025-63837-w.

Correspondence and requests for materials should be addressed to Guillermo Mínguez Espallargas.

Peer review information *Nature Communications* thanks Satoshi Horike, Hoi Ri Moon, Lothar Wondraczek and the other, anonymous, reviewer(s) for their contribution to the peer review of this work. A peer review file is available.

Reprints and permissions information is available at http://www.nature.com/reprints

Publisher's note Springer Nature remains neutral with regard to jurisdictional claims in published maps and institutional affiliations.

Open Access This article is licensed under a Creative Commons Attribution-NonCommercial-NoDerivatives 4.0 International License, which permits any non-commercial use, sharing, distribution and reproduction in any medium or format, as long as you give appropriate credit to the original author(s) and the source, provide a link to the Creative Commons licence, and indicate if you modified the licensed material. You do not have permission under this licence to share adapted material derived from this article or parts of it. The images or other third party material in this article are included in the article's Creative Commons licence, unless indicated otherwise in a credit line to the material. If material is not included in the article's Creative Commons licence and your intended use is not permitted by statutory regulation or exceeds the permitted use, you will need to obtain permission directly from the copyright holder. To view a copy of this licence, visit http://creativecommons.org/licenses/by-nc-nd/4.0/.

© The Author(s) 2025